Investigating Neutrino Oscillations at Astrophyscial Energy Scales

Bachelor Thesis

Written by *Franciszek Nawrocki*

June 14, 2024

Supervised by
Mauricio Bustamante & Bernanda Telalovic

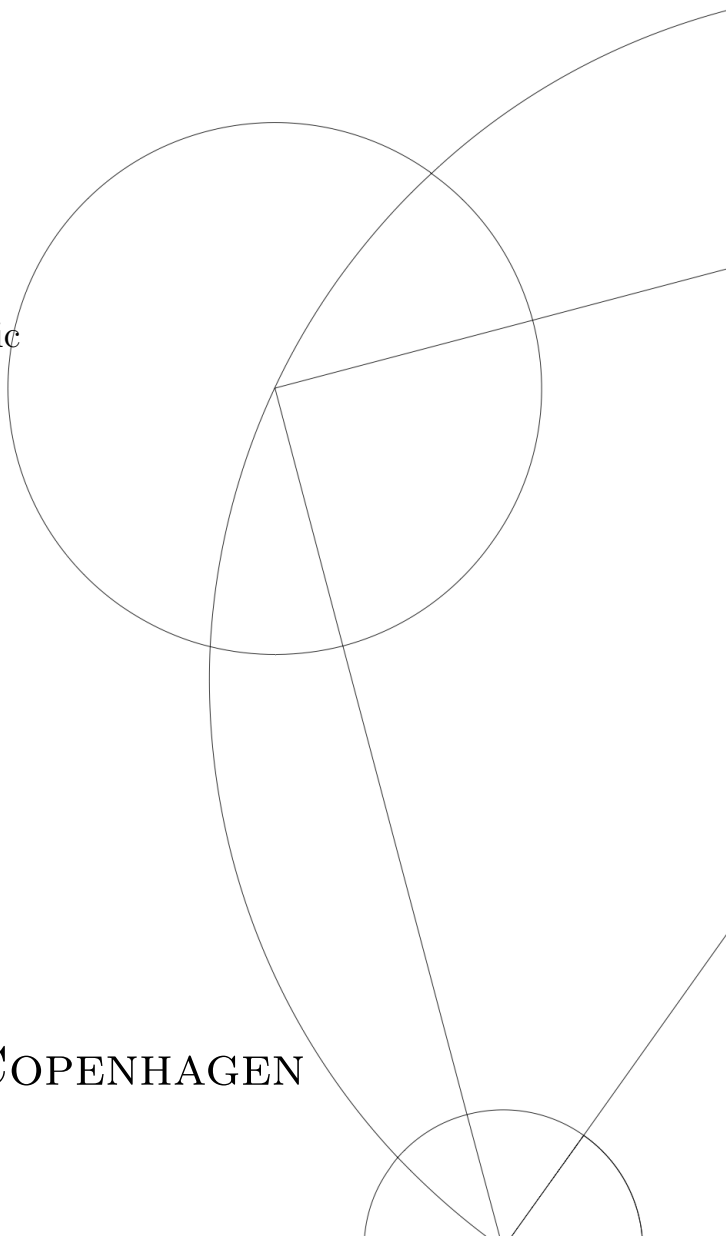

University of Copenhagen

UNIVERSITY OF COPENHAGEN

Name of Institute:	Niels Bohr Institute
Name of Department:	Astro Particle Physics
Author(s):	Franciszek Nawrocki
Email:	rth504@alumni.ku.dk
Title:	Investigating Neutrino Oscillations at Astrophyscial Energy Scales
Supervisor(s):	Mauricio Bustamante & Bernanda Telalovic
Handed in:	14.06.2024
Defended:	

Name _____

Signature _____

Date _____

Abstract

Neutrinos interact in flavour eigenstates but propagate through space in mass eigenstates. This leads to neutrino oscillations governed by the mixing matrix U. In the Standard Model, it is unitary, i.e., neutrinos can only mix between ν_e, ν_μ and ν_τ. In this report we explore what happens if we assume a parametrization of U that allows for non-unitarity. We derive the probability formula used for determining the flavour composition of neutrinos as a function of propagation length and energy for the unitary and non-unitary case, as well as the average probability which applies to astrophysical neutrinos. We perform a Bayesian analysis with UltraNest using projected data from IceCube to determine posterior distributions for the parameters of U in the LMM parametrization and for the astrophysical source flavour composition. We also investigate whether non-unitarity could come from a single row or column. From this, we compute the unitarity relations of U to investigate how close it is to being unitary.

The results of the analysis are compatible with unitarity of U at 68% confidence.

Acknowledgements

I would like to thank Mauricio Bustamante and Bernanda Telalovic for being really great supervisors, for making the process really enjoyable and especially for always being available to answer all the questions I might have had.

Contents

1 Introduction

Neutrinos are among the most mysterious particles in our universe. Due to their tiny mass and infrequent interactions, they were some of the last elementary particles to be discovered. All neutrinos exist as a superposition of flavour eigenstates which can mix into each other. This is represented by a mixing matrix. Assuming this matrix is unitary, neutrinos can only mix into the three known neutrino flavours. So far, the unitarity of this matrix has been tested up to the GeV-energy scale. Were one to expand this assumption to a non-unitary matrix we could possibly see neutrino mixing into hitherto unknown neutrino flavours. In this report we will be testing this assumption at greater than GeV-energy scales using astrophysical neutrinos.

2 Theory

Neutrinos are fermions, have no electric charge, and are part of the 12 spin-1/2 particles in the Standard Model (SM). The SM cosists of six quarks and six leptons (and their antiparticles) organized in three different families called flavours. They interact only through the weak force and gravity. The different neutrinos are the electron neutrino, ν_e, the muon neutrino, ν_μ, and the tau neutrino, ν_τ, and are each associated to their corresponding lepton, the electron, e, the muon, μ, and the tau, τ. That a neutrino is associated to its corresponding lepton means that a neutrino of a given flavour α only interacts weakly with leptons of the same flavour α. An example of such an interaction is pictured in Fig. 1.

Neutrinos are massive particles although their masses are yet to be determined precisely as they are several orders of magnitude smaller than any massive particle, we know so far. A neutrino of a given flavour is not a particle state with a well-defined mass, but a superposition of different of mass states. Each flavour state can be described as a coherent superposition of the mass states, ν_i where $i = 1, 2, 3$:

$$|\nu_\alpha\rangle = \sum_i U^*_{\alpha i} |\nu_i\rangle , \tag{1}$$

where α ranges over the flavours e, μ, τ and U is a unitary, complex mixing matrix. Likewise, by inverting the previous expression, each mass eigenstate is a superposition of flavour eigenstates:

$$|\nu_i\rangle = \sum_\alpha U_{\alpha i} |\nu_\alpha\rangle . \tag{2}$$

The unitarity of U,

$$UU^\dagger = \mathbb{1}, \tag{3}$$

guarantees that the neutrinos can only oscillate between the three known flavours and therefore also are only superpositions of the known flavours.

We consider some process that produces neutrinos of some specific flavour. This happens by the creation of a charged lepton of some flavour α. Alongside this, a neutrino is created. We then say the neutrino is of flavour α. To determine the flavour of the neutrino at a neutrino detector one measures the flavour of the charged lepton that the neutrino produces upon reacting with the detector material. If this charged lepton is of flavour β one says the neutrino also is of flavour β. In the case that $\alpha \neq \beta$ the neutrino has oscillated from flavour α to β. This is illustrated in the upper part of Fig. 1.

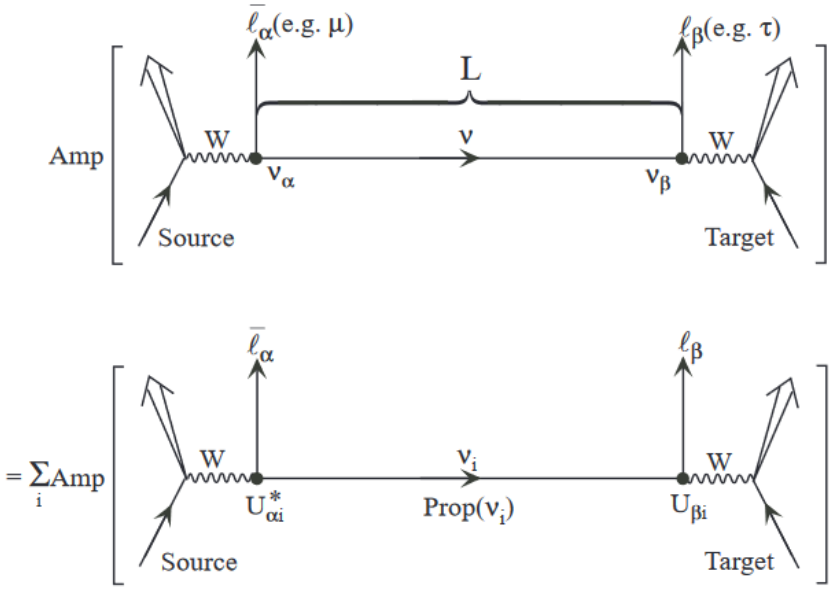

Figure 1: *Neutrino interaction and flavour change. Figure taken from Ref. [1].*

2.1 Neutrino Oscillations

To determine how the neutrinos oscillate between flavours we need to consider the probability amplitudes between the states. The fraction of a given flavour of a mass state is given by the amplitude squared $|U_{\alpha i}|^2$. Because the neutrinos propagate as waves they have a certain quantum mechanical phase. When considering oscillations over some travelled distance L we need to take into account the change of phase over this distance. The probability of oscillation is then

$$P(\nu_\alpha \to \nu_\beta) = \sum_i U^*_{\alpha i} \mathrm{Prop}(\nu_i) U_{\beta i}, \tag{4}$$

where $\mathrm{Prop}(\nu_i)$ denotes the phase accrued by the i-th mass eigenstate over the travelled distance L; see Fig. 1. The sum over i is because each flavour is a superposition of all three mass states. To find out what $\mathrm{Prop}(\nu_i)$ is let us consider the Schrödinger equation of the neutrino in its own rest frame in the mass basis and solve it:

$$i\frac{\partial}{\partial_{\tau_i}} |\nu_i(\tau_i)\rangle = m_i |\nu_i(\tau_i)\rangle \implies |\nu_i(\tau_i)\rangle = \exp(-im_i\tau_i) |\nu_i(0)\rangle . \tag{5}$$

The amplitude for travelling some time τ_i is $\langle\nu_i(0)|\nu_i(\tau_i)\rangle = \exp(-im_i\tau_i)$. We now want to express Eq. (5) in the laboratory time frame. Using the Lorentz transformations, we get

$$m_i\tau_i = E_i t - p_i L, \tag{6}$$

in natural units, $\hbar = 1$, $c = 1$. Because all neutrinos with energies different from each other pick up relative phase factors they average out and we only get one value of the energy. We can thus disregard the subscript on the energy, $E_i \to E$. In our analysis we will only consider astrophysical neutrinos with ultrarelativistic velocities. It thus applies to them that $E \gg m_i$. In this limit $p_i = \sqrt{E^2 - m_i^2} \approx \frac{1}{2}E(1 - \frac{m_i^2}{E^2})$. Putting

this back into our formula, $m_i\tau_i = E(t-L) + \frac{m_i^2}{2E}L$, and removing the common phase factor we finally have

$$\text{Prop}(\nu_i) = \exp\left(-im_i^2\frac{L}{2E}\right). \tag{7}$$

Denoting the amplitude of oscillation as $\text{Amp}(\nu_\alpha \to \nu_\beta)$ we have

$$\text{Amp}(\nu_\alpha \to \nu_\beta) = \sum_i U_{\alpha i}^* \exp\left(-im_i^2\frac{L}{2E}\right) U_{\beta i}. \tag{8}$$

Squaring the above we get the probability. We will derive the formula in section 2.2.

2.2 Derivation of Oscillation Probabilities

For the derivation we will show how to reach the final equation for the probability by squaring the amplitude. We start with

$$P(\nu_\alpha \to \nu_\beta) = |\text{Amp}(\nu_\alpha \to \nu_\beta)|^2 = \sum_i U_{\alpha i}^* \exp\left(-im_i^2\frac{L}{2E}\right) U_{\beta i} \sum_j U_{\alpha j} \exp\left(im_j^2\frac{L}{2E}\right) U_{\beta j}^*. \tag{9}$$

Let us first manipulate the above equation, Eq. (9):

$$P(\nu_\alpha \to \nu_\beta) = \sum_{i,j} U_{\alpha i}^* U_{\beta i} U_{\alpha j} U_{\beta j}^* \exp(-i\Delta m_{ij}^2 \frac{L}{2E}) \tag{10}$$

$$= \sum_{i,j} U_{\alpha i}^* U_{\beta i} U_{\alpha j} U_{\beta j}^* \left[1 - 2\sin^2(\Delta m_{ij}^2 \frac{L}{4E}) - i\sin(\Delta m_{ij}^2 \frac{L}{2E})\right] \tag{11}$$

$$\begin{aligned} = &\sum_{i=j} U_{\alpha i}^* U_{\beta i} U_{\alpha j} U_{\beta j}^* + \sum_{i>j} U_{\alpha i}^* U_{\beta i} U_{\alpha j} U_{\beta j}^* \left[1 - 2\sin^2(\Delta m_{ij}^2 \frac{L}{4E}) - i\sin(\Delta m_{ij}^2 \frac{L}{2E})\right] \\ &+ \sum_{j>i} U_{\alpha i}^* U_{\beta i} U_{\alpha j} U_{\beta j}^* \left[1 - 2\sin^2(\Delta m_{ij}^2 \frac{L}{4E}) - i\sin(\Delta m_{ij}^2 \frac{L}{2E})\right], \end{aligned} \tag{12}$$

where Δm_{ij}^2 denotes the mass squared difference $m_i^2 - m_j^2$. The first term does not contain any trigonometric functions because if $i = j$ then $\Delta m_{ij}^2 = 0$ which makes the trigonometric functions cancel out.

Let us first evaluate the terms not involving trigonometric functions in Eq. (12):

$$\begin{aligned} &\sum_{i=j} U_{\alpha i}^* U_{\beta i} U_{\alpha j} U_{\beta j}^* + \sum_{i>j} U_{\alpha i}^* U_{\beta i} U_{\alpha j} U_{\beta j}^* + \sum_{j>i} U_{\alpha i}^* U_{\beta i} U_{\alpha j} U_{\beta j}^* \\ = &\sum_{i=j} U_{\alpha i}^* U_{\beta i} U_{\alpha j} U_{\beta j}^* + \sum_{i>j} \left[\Re(U_{\alpha i}^* U_{\beta i} U_{\alpha j} U_{\beta j}^*) + \Im(U_{\alpha i}^* U_{\beta i} U_{\alpha j} U_{\beta j}^*)\right] \\ &+ \sum_{j>i} \left[\Re(U_{\alpha i}^* U_{\beta i} U_{\alpha j} U_{\beta j}^*) + \Im(U_{\alpha i}^* U_{\beta i} U_{\alpha j} U_{\beta j}^*)\right] \end{aligned} \tag{13}$$

$$= \sum_{i=j} U_{\alpha i}^* U_{\beta i} U_{\alpha j} U_{\beta j}^* + \sum_{i>j} \left[\Re(U_{\alpha i}^* U_{\beta i} U_{\alpha j} U_{\beta j}^*)\right] + \sum_{j>i} \left[\Re(U_{\alpha i}^* U_{\beta i} U_{\alpha j} U_{\beta j}^*)\right]. \tag{14}$$

In the third equality the two imaginary parts cancel out. To see this consider Eq. (15) where we have written down the two imaginary parts from Eq. (13):

$$\begin{aligned}
&\sum_{i>j} \Im(U^*_{\alpha i} U_{\beta i} U_{\alpha j} U^*_{\beta j}) + \sum_{j>i} \Im(U^*_{\alpha i} U_{\beta i} U_{\alpha j} U^*_{\beta j}) \\
=&\sum_{i>j} \Im(U^*_{\alpha i} U_{\beta i} U_{\alpha j} U^*_{\beta j}) + \sum_{i>j} \Im(U^*_{\alpha j} U_{\beta j} U_{\alpha i} U^*_{\beta i}) \\
=&\sum_{i>j} \Im(U^*_{\alpha i} U_{\beta i} U_{\alpha j} U^*_{\beta j}) + \sum_{i>j} \left(\Im(U_{\alpha j} U^*_{\beta j} U^*_{\alpha i} U_{\beta i})\right)^* = 0.
\end{aligned} \tag{15}$$

In the first equality in the second term, we have switched $i \leftrightarrow j$. In the second equality we have complex conjugated the second term twice. The third equality follows because the two terms are complex conjugates of each other, and they are purely imaginary.

The first term of Eq. (14) can now be written as follows:

$$\sum_{i=j} U^*_{\alpha i} U_{\beta i} U_{\alpha j} U^*_{\beta j} = \sum_{i,j} U^*_{\alpha i} U_{\beta i} U_{\alpha j} U^*_{\beta j} - \sum_{i>j} U^*_{\alpha i} U_{\beta i} U_{\alpha j} U^*_{\beta j} - \sum_{j>i} U^*_{\alpha i} U_{\beta i} U_{\alpha j} U^*_{\beta j} \tag{16}$$

$$= \sum_{i,j} U^*_{\alpha i} U_{\beta i} U_{\alpha j} U^*_{\beta j} - \sum_{i>j} \Re(U^*_{\alpha i} U_{\beta i} U_{\alpha j} U^*_{\beta j}) - \sum_{j>i} \Re(U^*_{\alpha i} U_{\beta i} U_{\alpha j} U^*_{\beta j}) \tag{17}$$

$$= \sum_{i,j} U^*_{\alpha i} U_{\beta i} U_{\alpha j} U^*_{\beta j} - 2\sum_{i>j} \Re(U^*_{\alpha i} U_{\beta i} U_{\alpha j} U^*_{\beta j}). \tag{18}$$

We collected the two real terms for a similar reason as in Eq. (15). Following that argument, the terms are complex conjugates of each other. Because they are purely real, they add. Inserting Eq. (18) into Eq. (14) we are left with:

$$\sum_{i,j} U^*_{\alpha i} U_{\beta i} U_{\alpha j} U^*_{\beta j} = \sum_i U^*_{\alpha i} U_{\beta i} \sum_j U_{\alpha j} U^*_{\beta j} = \delta_{\alpha\beta}\delta_{\alpha\beta} = \delta_{\alpha\beta}. \tag{19}$$

The $\delta_{\alpha\beta}$ emerges in Eq. (19) because we assume U is unitary. Inserting this back into Eq. (12) we have

$$\begin{aligned}
P(\nu_\alpha \to \nu_\beta) = \delta_{\alpha\beta} &+ \sum_{i>j} U^*_{\alpha i} U_{\beta i} U_{\alpha j} U^*_{\beta j} \left[-2\sin^2(\Delta m^2_{ij}\frac{L}{4E}) - i\sin(\Delta m^2_{ij}\frac{L}{2E})\right] \\
&+ \sum_{j>i} U^*_{\alpha i} U_{\beta i} U_{\alpha j} U^*_{\beta j} \left[-2\sin^2(\Delta m^2_{ij}\frac{L}{4E}) - i\sin(\Delta m^2_{ij}\frac{L}{2E})\right] \\
= \delta_{\alpha\beta} &- 4\sum_{i>j} \Re(U^*_{\alpha i} U_{\beta i} U_{\alpha j} U^*_{\beta j}) \sin^2(\Delta m^2_{ij}\frac{L}{4E}) \\
&+ 2\sum_{i>j} \Im(U^*_{\alpha i} U_{\beta i} U_{\alpha j} U^*_{\beta j}) \sin(\Delta m^2_{ij}\frac{L}{2E}),
\end{aligned} \tag{20}$$

where we have used the same argument as in Eq. (15). The real parts of U's are even under the interchange of $i \leftrightarrow j$, as is $\sin^2$, so they add. The imaginary parts of U's are odd under the interchange of $i \leftrightarrow j$, as is sin, so they add. All other terms vanish.

The probability formula assuming unitarity is thus derived and written below:

$$\begin{aligned} P(\nu_\alpha \to \nu_\beta) = \delta_{\alpha\beta} &- 4\sum_{i>j} \Re(U^*_{\alpha i}U_{\beta i}U_{\alpha j}U^*_{\beta j}) \sin^2(\Delta m^2_{ij}\frac{L}{4E}) \\ &+ 2\sum_{i>j} \Im(U^*_{\alpha i}U_{\beta i}U_{\alpha j}U^*_{\beta j}) \sin(\Delta m^2_{ij}\frac{L}{2E}). \end{aligned} \tag{21}$$

Likewise, the non-unitary case follows the same line of reasoning except the assumption of unitarity in Eq. (19). Therefore, we revert back this step and we keep $\sum_{i,j} U^*_{\alpha i}U_{\beta i}U_{\alpha j}U^*_{\beta j}$ instead of $\delta_{\alpha\beta}$ in Eq. (21). This brings us to the oscillation probability for the non-unitary case:

$$\begin{aligned} P_{\rm NU}(\nu_\alpha \to \nu_\beta) &= \sum_{i,j} U^*_{\alpha i}U_{\beta i}U_{\alpha j}U^*_{\beta j} - 4\sum_{i>j} \Re(U^*_{\alpha i}U_{\beta i}U_{\alpha j}U^*_{\beta j}) \sin^2(\Delta m^2_{ij}\frac{L}{4E}) \\ &\quad + 2\sum_{i>j} \Im(U^*_{\alpha i}U_{\beta i}U_{\alpha j}U^*_{\beta j}) \sin(\Delta m^2_{ij}\frac{L}{2E}) \\ &= \left|\sum_i U^*_{\alpha i}U_{\beta i}\right|^2 - 4\sum_{i>j} \Re(U^*_{\alpha i}U_{\beta i}U_{\alpha j}U^*_{\beta j}) \sin^2(\Delta m^2_{ij}\frac{L}{4E}) \\ &\quad + 2\sum_{i>j} \Im(U^*_{\alpha i}U_{\beta i}U_{\alpha j}U^*_{\beta j}) \sin(\Delta m^2_{ij}\frac{L}{2E}). \end{aligned} \tag{22}$$

Let us also derive the probability formula for the average probability for very large L/E. This is because the astrophysical neutrinos which we will be considering have energies in the range 10^5GeV and travel distances of the order of parsecs [2]. In this regime the function oscillates fast enough so that we can, for all practical purposes, consider it averaged over L/E. Let the starting point be the second expression in Eq. (22):

$$\begin{aligned} &\bar{P}(\nu_\alpha \to \nu_\beta) \\ &= \sum_{i,j} U^*_{\alpha i}U_{\beta i}U_{\alpha j}U^*_{\beta j} - 4\sum_{i>j} \Re(U^*_{\alpha i}U_{\beta i}U_{\alpha j}U^*_{\beta j}) \sin^2(\Delta m^2_{ij}\frac{L}{4E}) + 2\sum_{i>j} \Im(U^*_{\alpha i}U_{\beta i}U_{\alpha j}U^*_{\beta j}) \sin(\Delta m^2_{ij}\frac{L}{2E}) \\ &= \sum_{i,j} U^*_{\alpha i}U_{\beta i}U_{\alpha j}U^*_{\beta j} - 4\sum_{i>j} \Re(U^*_{\alpha i}U_{\beta i}U_{\alpha j}U^*_{\beta j})\frac{1}{2} \\ &= \sum_{i=j} U^*_{\alpha i}U_{\beta i}U_{\alpha j}U^*_{\beta j} + \sum_{i>j} U^*_{\alpha i}U_{\beta i}U_{\alpha j}U^*_{\beta j} + \sum_{j>i} U^*_{\alpha i}U_{\beta i}U_{\alpha j}U^*_{\beta j} - 2\sum_{i>j} \Re(U^*_{\alpha i}U_{\beta i}U_{\alpha j}U^*_{\beta j}) \\ &= \sum_{i=j} U^*_{\alpha i}U_{\beta i}U_{\alpha j}U^*_{\beta j} \\ &= \sum_i |U_{\alpha i}|^2|U_{\beta i}|^2, \end{aligned} \tag{23}$$

where we have used the fact that $\sin^2(\Delta m^2_{ij}\frac{L}{4E})$ averages to $\frac{1}{2}$ whilst $\sin(\Delta m^2_{ij}\frac{L}{2E})$ averages to 0. Due to the same argument as in Eq. (15), the imaginary parts of the two middle terms cancel each other whilst the real part from these terms cancel the last term.

We have thus deduced the average oscillation probability and will write it again for clarity,

$$\bar{P}(\nu_\alpha \to \nu_\beta) = \sum_i |U_{\alpha i}|^2 |U_{\beta i}|^2. \tag{24}$$

The last equation was derived without making any assumptions on the unitarity of U.

All three oscillation probability formulas, Eqs. (21), (22), (24), will be used later for performing calculations.

2.3 Flavour composition of high-energy astrophysical neutrinos

We construct a probability matrix containing in each entry the average probability from the initial flavour to the final flavour,

$$\bar{\boldsymbol{P}} = \begin{bmatrix} \bar{P}_{ee} & \bar{P}_{e\mu} & \bar{P}_{e\tau} \\ \bar{P}_{\mu e} & \bar{P}_{\mu\mu} & \bar{P}_{\mu\tau} \\ \bar{P}_{\tau e} & \bar{P}_{\tau\mu} & \bar{P}_{\tau\tau} \end{bmatrix}. \tag{25}$$

We will introduce the flavour composition emitted by a neutrino source and detected later at a detector i.e. the ratio of the flux, Φ, of a given flavour to the total flux of neutrinos. For ν_e, ν_μ, ν_τ respectively we have $f_e = \Phi_e/\Phi_{\text{total}}$, $f_\mu = \Phi_\mu/\Phi_{\text{total}}$, $f_\tau = \Phi_\tau/\Phi_{\text{total}}$. These are collected in a vector to construct the flavour ratio vector,

$$\boldsymbol{f} = \begin{bmatrix} f_e \\ f_\mu \\ f_\tau \end{bmatrix}.$$

The flavour ratio measurement at Earth given some flavour ratio at the neutrino source is calculated using the average probability matrix,

$$\boldsymbol{f}_\oplus = \bar{\boldsymbol{P}} \boldsymbol{f}_S, \tag{26}$$

where $\boldsymbol{f}_\oplus$ is the flavour ratio vector measured at the Earth and $\boldsymbol{f}_S$ is the flavor ratio vector emitted by the source.

For our later analysis we will need to supply best-fit values for the measured flavour composition at the Earth. We will be using projected future values, but the measurements are made by Ice Cube by detecting three different event topologies: Cascades, tracks, and double cascades. They are each attributed to the flavour of incoming neutrino and interaction type. Charged-current (CC) interactions with ν_e produce single cascades. CC interactions with ν_μ produce tracks while CC interactions with ν_τ produce double cascades. Neutral current interactions with all flavours produce single cascades. The projected values we will be working with assume the location of a pion-decay flavour composition measurement [3].

These are projected values for 2040 using data from various experiments including IceCube and oscillation parameters from data from various experiments. The values are taken from Table 2 in [4].

$$\begin{aligned} \bar{f}_{e,\oplus} &= 0.30 \pm 0.030 \\ \bar{f}_{\mu,\oplus} &= 0.36 \pm 0.011 \end{aligned} \tag{27}$$

The covariance matrix of these two measurements contains the uncertainties of them on the diagonal and their correlations on the off-diagonal. Although probably not the

case in reality, we assume the measurements are uncorrelated. The covariance matrix then takes the form:

$$\sigma = \begin{bmatrix} 0.030 & 0 \\ 0 & 0.011 \end{bmatrix}. \tag{28}$$

In our later analysis we will be using a toy model for the flavour measurement: A gaussian distribution in $f_{e,\oplus}$ and $f_{\mu,\oplus}$, centred at the values in Eq. (27). This form is meant to approximate the sensitivity to flavour-composition measurements achieved by combining upcoming neutrino telescopes. We will cover this in section 3.2.

We only need to specify $f_{e,\oplus}$ and $f_{\mu,\oplus}$ because $f_{\tau,\oplus}$ is given by $1 - f_{e,\oplus} - f_{\mu,\oplus}$.

2.4 Matrix Parametrizations

When working with a unitary 3x3 matrix we are free to choose its parametrization. In general, this has 9 real parameters although for our case 5 of them are unnecessary as they do not influence neutrino oscillations [5]. For this report we will be working mostly with the form shown below, U_{PMNS}. This is the standard parametrization used for the neutrino mixing matrix [6]. Usually, one includes terms involving Majorana and CP-violating phases but as these do not have influence on neutrino oscillations we do not need to consider them. We use:

$$U_{\text{PMNS}} = \begin{bmatrix} 1 & 0 & 0 \\ 0 & c_{23} & s_{23} \\ 0 & -s_{23} & c_{23} \end{bmatrix} \begin{bmatrix} c_{13} & 0 & s_{13}e^{-i\delta_{\text{CP}}} \\ 0 & 1 & 0 \\ -s_{13}e^{i\delta_{\text{CP}}} & 0 & c_{13} \end{bmatrix} \begin{bmatrix} c_{12} & s_{12} & 0 \\ -s_{12} & c_{12} & 0 \\ 0 & 0 & 1 \end{bmatrix}, \tag{29}$$

where $c_{ij} \equiv \cos\theta_{ij}$ and $s_{ij} \equiv \sin\theta_{ij}$ and δ_{CP} is a CP-violating phase [1]. The three angles along with δ_{CP} constitute the four parameters necessary to describe a unitary 3x3 matrix.

In this report we will investigate non-unitarity. In this case we need a new parametrization that does not assume the matrix to be unitary. In general, such a matrix has 18 parameters as each entry takes complex values. Again, 5 of these account for Majorana phases and charged lepton fields [7], these we can disregard in our analysis as they have no influence on neutrino oscillations. We thus choose the LMM parametrization [7], U_{LMM}, for our non-unitary mixing matrix,

$$U_{\text{LMM}} = \begin{pmatrix} |U_{e1}| & |U_{\mu 1}|e^{i\phi_{e2}} & |U_{\tau 1}|e^{i\phi_{e3}} \\ |U_{e2}| & |U_{\mu 2}| & |U_{\tau 2}| \\ |U_{e3}| & |U_{\mu 3}|e^{i\phi_{\tau 2}} & |U_{\tau 3}|e^{i\phi_{\tau 3}} \end{pmatrix}. \tag{30}$$

It includes 9 real, positive-valued moduli of the entries as well as 4 phases.

For parts of our analysis further on we will need to supply values for the different parametrization parameters. For U_{PMNS} we will be using global best-fit values from NuFIT 5.1 [8]. They are $\theta_{12} = 33.44°$, $\theta_{13} = 8.57°$, $\theta_{23} = 49.2°$ and $\delta_{\text{CP}} = 194°$. These data are collected from a range of experiments. Furthermore, we will be using the best-fit values for the mass splittings also from NuFIT 5.1, [8]. These are based on the same experiments as the above values for the parameters of U_{PMNS}. They are $\Delta m^2_{21} = 7.42 \cdot 10^{-5}\text{eV}^2$, $\Delta m^2_{31} = 2.515 \cdot 10^{-3}\text{eV}^2$ and $\Delta m^2_{32} = \Delta m^2_{31} - \Delta m^2_{21}$. These values for the mass squared splittings will be used in all simulations performed with the probability formulas, Eqs. (21), (22).

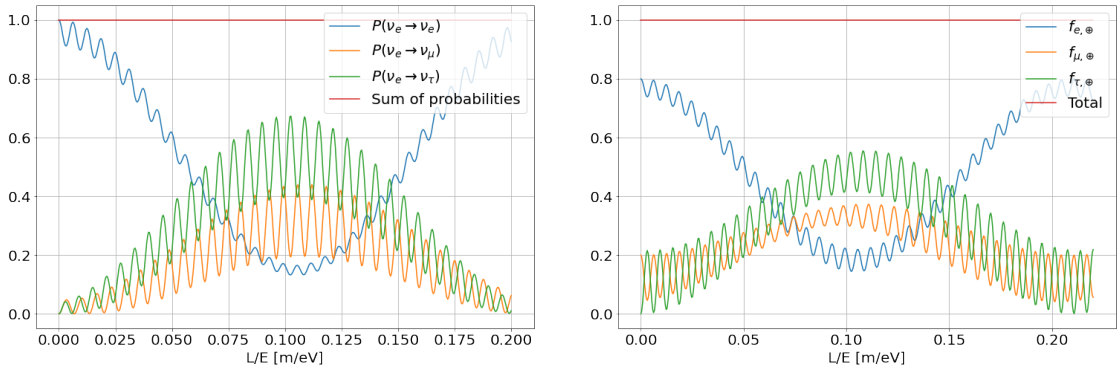

Figure 2: Left: *Transition probability, Eq. (21), as a function of* L/E. Right: *Flavour composition as a function of* L/E *with initial flavour composition* $[0.8, 0.2, 0]$. *This choice has no greater implication but was chosen such that it illustrates the behaviour of the function.*

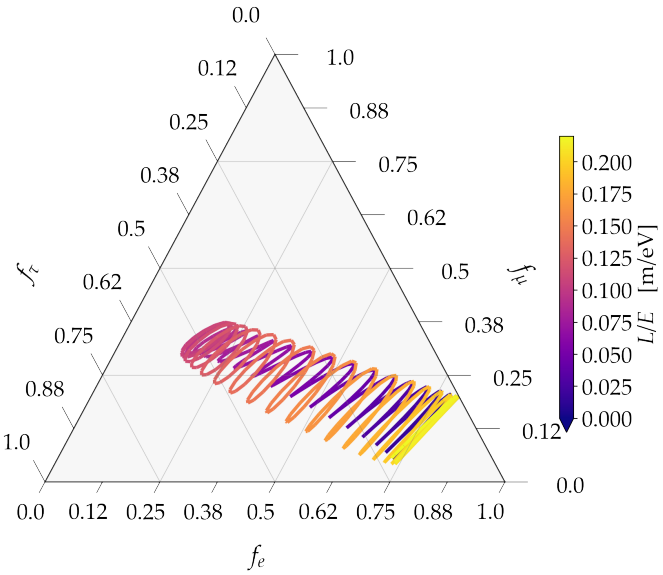

Figure 3: *Flavour composition as a function of* L/E *with initial flavour composition* $[0.8, 0.2, 0]$ *represented in a ternary plot. This choice has no greater implication but was chosen such that it illustrates the behaviour of the function.*

Fig. 2 (left) shows the behaviour of the unitary probability formula, Eq. (21), as a function of L/E using the above best-fit values for U_{PMNS}. In the plot, we see oscillations of different frequencies. The small mass squared differences drive the oscillations of lowest frequency i.e. the long ones for which we see one period. The greatest values of the mass squared differences drive the small frequent oscillations. The red line at the top is the sum of probabilities, which never exceeds 1, reflecting the unitarity of U.

Fig. 2 (right) shows the corresponding flavour content of a flux of neutrinos as they propagate and oscillate. This also uses the above values for U_{PMNS}. It is dependent on

an initial flavour ratio in this case chosen to be $[0.8, 0.2, 0]$. In effect, this only decides where the three curves begin at $L/E = 0$ and was chosen such that the behaviour of the probability formula is best demonstrated.

Fig. 3 shows the same the same physics as Fig. 2 in a ternary plot. On the three axes are the three different flavour ratios. Because f_τ is determined by the values of f_e and f_μ as $f_\tau = 1 - (f_e + f_\mu)$ the three quatities can be represented in a 2D plot. The initial flavour ratio again is $[0.8, 0.2, 0]$. The pattern shown is exactly the oscillations from Fig. 2 (right). The pattern overlaps as many times as it does thanks to the rapid oscillations also seen in Fig. 2. For different initial flavour ratios, the points would fill in the triangle differently.

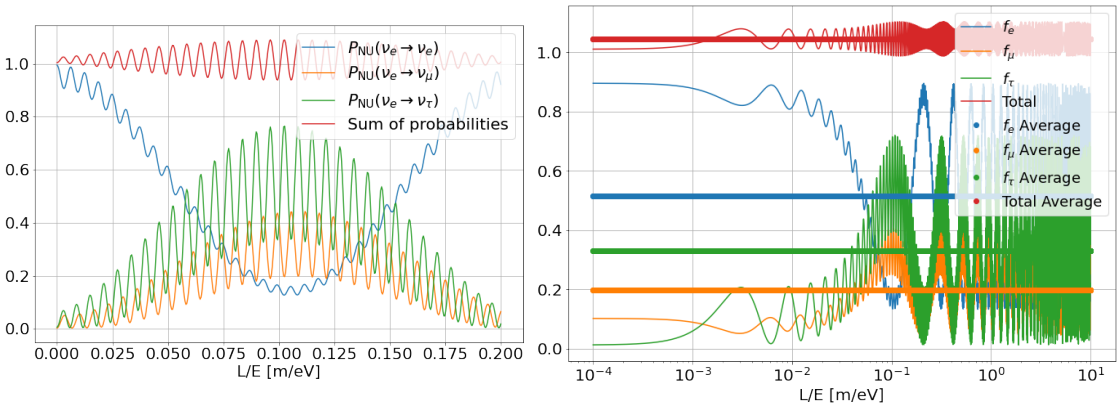

Figure 4: Left: *Transition probability, Eq. (22), as a function of L/E for a non-unitary U.* Right: *Flavour composition as a function of L/E with initial flavour composition* $[0.9, 0.1, 0]$ *for a non-unitary U. This choice has no greater implication but was chosen such that it illustrates the behaviour of the function. Straight lines are computed using the average probability formula, Eq. (24).* In both plots we used the above values for U_{PMNS} except we manually set $U_{33} = 0.4$. The specific value was chosen to illustrate the effect of non-unitarity.

In Fig. 4 (left) we have introduced non-unitarity to U by setting $U_{33} = 0.4$. The full U used for this plot is:

$$U_{\mathrm{PMNS,NU}} = \begin{bmatrix} 0.83 & 0.55 & -0.14+0.04i \\ -0.27+0.02i & 0.61+0.02i & 0.75 \\ 0.50+0.02i & -0.58+0.01i & 0.4 \end{bmatrix}. \tag{31}$$

This is the U_{PMNS} parametrization using the best-fit values with U_{33} manually set to 0.4. For the non-unitary U the transition probability exceeds and subceeds 1 depending on L/E, as expected. This was calculated using Eq. (22). Physically, a probability above 1 would indicate that a potential fourth neutrino flavour could oscillate into one of the three known flavours. Likewise, a probability below 1 indicates that we lose a fraction of the known flavours to a fourth flavour. Were we to take the fourth flavour into account in our analysis, the total probability would again sum up to 1.

Fig. 4 (right) compares the flavour ratio computed using the oscillation probability formula for a non-unitary U, Eq. (22), to the oscillation probability computed using the average probability formula, Eq. (24). Again, we use the mixing matrix from Eq. (31). Moreover, the logarithmic x-axis shows that at L/E-scales above $\sim$ 10m/eV,

oscillations are so fast that we must turn to the averages. This is the case for astrophysical neutrinos as these travel distances of the order of parsecs on their way to the Earth. We show this with a calculation, 1pc $\approx 10^{16}$m so $\frac{10^{16}\text{m}}{10^5\text{GeV}} = 10^2 \frac{\text{m}}{\text{eV}}$, which is in the appropriate range [2].

Next, we deal with the average probability being above 1 by introducing renormalization (RN) i.e. we rescale $f_{e,\text{RN}} = f_e/(f_e + f_\mu + f_\tau)$ and likewise for f_μ and f_τ. This is how the flavour composition is measured at IceCube.

The best-fit parameters we have worked with so far will also be used for the analysis performed with UltraNest.

For another demonstration we will use the data from NuFIT 5.0, taken from Table 1 in Ref. [4]. They are reported at 68% confidence. In Ref. [4] they are reported with an upper bound and lower bound. For all parameters we have taken the numerically bigger one,

$$\begin{aligned} \sin^2\theta_{12} &= 0.304 \pm 0.012 \\ \sin^2\theta_{13} &= 0.02219 \pm 0.00063 \\ \sin^2\theta_{23} &= 0.573 \pm 0.020 \\ \delta_{CP} &= 197.0^\circ \pm 27^\circ. \end{aligned} \tag{32}$$

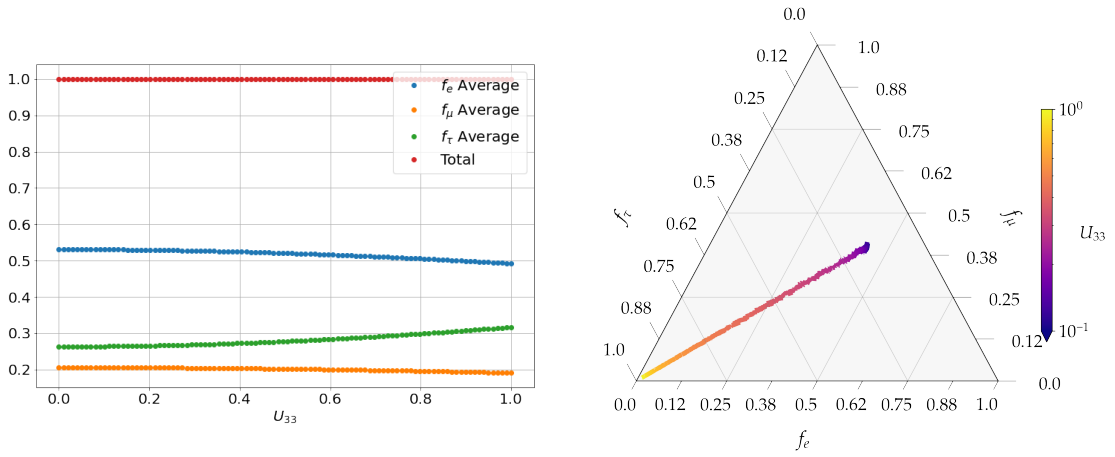

Figure 5: Flavour composition computed using the average probability formula, Eq. (24), renormalized to account for non-unitarity, plotted as a function of U_{33}. Left: *Demonstrated in a regular plot with U varying in the interval* $[0, 1]$. *Initial flavour composition is* $[0.9, 0.1, 0]$. Right: *Demonstrated in a ternary plot with U varying in the interval* $[10^{-1}, 10^0]$ *logarithmically. Initial flavour composition is* $[1/3, 2/3, 0]$.

Fig. 5 (left) shows average probabilities, Eq. (24), computed for each of the three known flavours as a function of U_{33} with the rest of the parameters taking the values in Eq. (31). The flavour compositions are renormalized such that the total stays at 1. The plot shows their relative behaviour. It is clear that as f_τ increases, relatively, both f_e and f_μ decrease. Physically, such behaviour could come from a fourth flavour oscillating only into ν_τ.

Fig. 5 (right) shows the average probability, Eq. (24), varying with U_{33}. The other components of U_{PMNS} are sampled from normal distributions using the values from Eq.

(32) as means and standard deviations. Due to this sampling the line in the plot has some width and texture to it. U_{33} is sampled logarithmically in the interval $[10^{-1}, 10^{0}]$ with 1000 points. The initial flavour ratio used in this simulation is $[1/3, 2/3, 0]$. This flavour ratio dictates the starting point of the line, i.e. the dark part of it. The flavour ratio is renormalized such that we see the relative change among the three neutrino flavours. The behaviour is, as expected, a line towards the point $f_\tau = 1$. The ratio of ν_τ relatively increases whilst the two others decrease at the same rate.

3 Methods

3.1 Analysis

The bulk of the analysis will consist of asking the question: What is the probability that certain matrix parameters and a specific flavour composition at the source give rise to a given measurement at the Earth. In practice, for this measurement at the Earth, we will use projected data. The statistical analysis will be performed with help from the analytical tool, UltraNest, to be described in section 3.2.

We will be performing two types of analyses. One where we vary all 13 matrix parameters in the LMM parametrization, Eq. (30), including the flavour composition at the source, $\boldsymbol{f}_S$, for a total of 14 parameters. We assume $\boldsymbol{f}_S$ takes the form $[f_{e,S}, 1 - f_{e,S}, 0]$ i.e. only ν_e and ν_μ are generated at the astrophysical source. This is a reasonable assumption given that the IceCube measurement, Eq. (27), reflects that of pion-decay at the source under standard oscillations and pion decay only produces ν_e and ν_μ [3]. Our parameter is then $f_{e,S}$. In this approach, we do not assume the non-unitarity comes in a specific entry, we are open to all possibilities. From this, we should be able to say something about all the parameters at the same time using the unitarity relations of the matrix, Eq. (3).

Furthermore, we will be running simulations where we vary only a single row or column of U at a time. In this case, when varying the parameters we will assume they take the shape of a complex number with an amplitude, $|U|$, and a phase, ϕ, $|U| \exp(i\phi)$. For the rest of the matrix, we will assume it takes the form of the U_{PMNS} matrix, with the best-fit values, top of section 2.4. This approach is more specific than varying all the parameters and amounts to constraining non-unitarity and mixing into a fourth flavour to only one row or column. For this analysis we will also let the flavour composition at the source be a parameter and vary freely.

3.2 Bayesian Statistics and UltraNest

The statistical aspect of the simulations will be based on Bayesian statistics through the analysis tool UltraNest. Let us briefly go through the basics of Bayes' theorem.

In short, Bayes' theorem tells us how to update our probabilities for some event given new evidence. This can be expressed as

$$P(H|E) = \frac{P(E|H)P(H)}{P(E)}, \tag{33}$$

where $P(H|E)$, the posterior, is the probability of some hypothesis H being true given some evidence E, $P(E|H)$, the likelihood, is the probability of the evidence being true given that the hypothesis is true, $P(H)$, the prior, is the total probability that the

hypothesis is true, without considering the extra evidence. Lastly, $P(E)$ is the total probability of the evidence being true in an isolated scenario without reference to the hypothesis [9]. Our analysis is based on this very principle.

Ultranest is a tool performing Bayesian inference which is a type of Bayesian analysis for continuous parameter distributions. It expands Bayes' theorem to continuous parameters. The probabilities above take the form of probability distributions instead. The Likelihood for the continuous case becomes a likelihood function. The prior becomes a prior distribution. To make the analysis work we need to supply the prior distributions of the model parameters to Ultranest as well as a likelihood function.

Our model parameters will be all components of U_{LMM}, Eq. 30, as well as the electron fraction of the flavour composition at the source, $f_{e,S}$. For all the elements $|U_{\alpha i}|$ we let them vary in the interval $[0, 1]$. This is because these are the allowed values for our parametrization. For all angles we let these vary in the interval $[0, 2\pi]$ as there are no constraints on these. We also vary $f_{e,S}$ in the interval $[0, 1]$. The Likelihood is computed as

$$\mathcal{L}(\boldsymbol{f}_\oplus, \bar{\boldsymbol{f}_\oplus}, \sigma) = \frac{1}{\sqrt{(2\pi)^2 \det\sigma}} \exp\left(-\frac{1}{2}(\boldsymbol{f}_\oplus - \bar{\boldsymbol{f}_\oplus})^T \sigma^{-1} (\boldsymbol{f}_\oplus - \bar{\boldsymbol{f}_\oplus})\right), \tag{34}$$

where $\boldsymbol{f}_\oplus = \bar{\boldsymbol{P}}(U)\boldsymbol{f}_S$, where $\boldsymbol{f}_S = [f_{e,S}, 1 - f_{e,S}, 0]$, $\bar{\boldsymbol{f}_\oplus}$ is the measured flavour composition at the Earth, that is, the values at which the distributions are centred, σ is the covariance matrix of the measurement. $\boldsymbol{f}_\oplus$ has been renormalized so that it is commensurable with the IceCube measurement. In practice we only supply the first two components of $\boldsymbol{f}_\oplus$ in Eq. (34) as f_τ is dependent on the other components.

That is, in our analysis we compare the measured values at Earth with the possible predictions by the probability formula assuming an initial flavour composition and matrix parameters using a 2D normal distribution for the measurement at the earth, where the flavour ratios f_e and f_μ are the two variables. The closer the predicted value to the measurement at the Earth the higher the likelihood. Then the parameters of U for which we get the highest likelihood will be reported as being the most probable. The same applies to $\boldsymbol{f}_S$, the value which generates the highest likelihood will be reported as the most probable. For the analysis we will be using the values from Eqs. (27) and (28).

To sum up, we compute the likelihood as in Eq. (34) using only the first two components of $\boldsymbol{f}_\oplus$ which is a predicted measurement at the earth computed for a certain U and $\boldsymbol{f}_S$, and measured IceCube values $\bar{\boldsymbol{f}_\oplus}$ with their corresponding covariance matrix σ. In practice, we compute the logarithm of the likelihood, $\log\mathcal{L}$.

4 Results

4.1 Posterior Probability Distributions

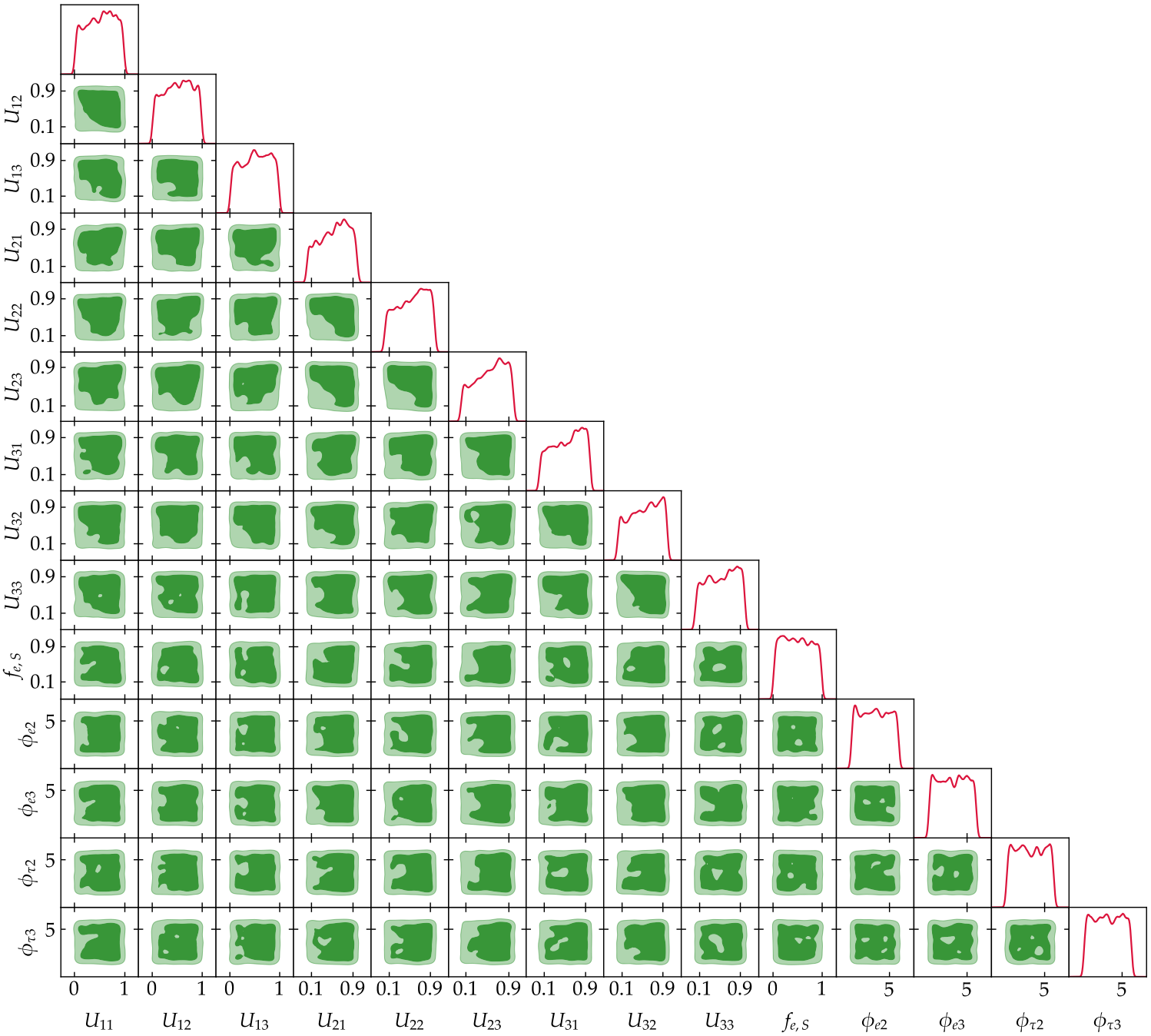

Figure 6: *Corner plot illustrating the posteriors of all 13 parameters in the LMM-parametrization of the neutrino mixing matrix, U, and the flavour composition at the source, $[f_{e,S}, 1 - f_{e,S}, 0]$. Histograms are posterior distributions of each parameter. Green plots are correlations between the individual parameters. Dark green regions are 68% confidence regions, light green regions are 95% confidence regions.*

Fig. 6 displays the posteriors of the UltraNest simulation when varying all 13 parameters of U in the LMM parametrization as well as the electron fraction of the initial

flavour composition $f_{e,S}$. The histograms in the top row of the triangle show posterior distributions for each model parameter, i.e., how many Monte Carlo samples exist within each bin. These do not necessarily reflect the best fit value when considering all of the parameters at the same time.

Each plot and histogram are shown with wider ranges than physically allowed. This is for reading clarity, the possible values of the parameters, i.e., the ranges for the parameters, are their prior distributions as explained in section 3.2. Some leakage outside of the specified ranges may occur. This is due to smoothing of the plots which is done to eliminate noise.

The green plots show the correlation between each pair of parameters. The dark green region is the allowed region at 68% confidence whereas the light green region is the allowed region at 95% confidence. The plots are telling us which values any pair of parameters can take on at the same time. As an example, take the correlation between $|U_{12}|$ and $|U_{11}|$. The parameters can take on any values at 95% confidence whereas the bottom left corner is excluded at 68% confidence. For ϕ_{e2} and $f_{e,S}$, the green regions covers the entire plot more or less uniformly. This means that there is no correlation between these two parameters, they can take on any value at the same time. In general, the smaller and more irregular the shape of the green region the more correlation between two parameters.

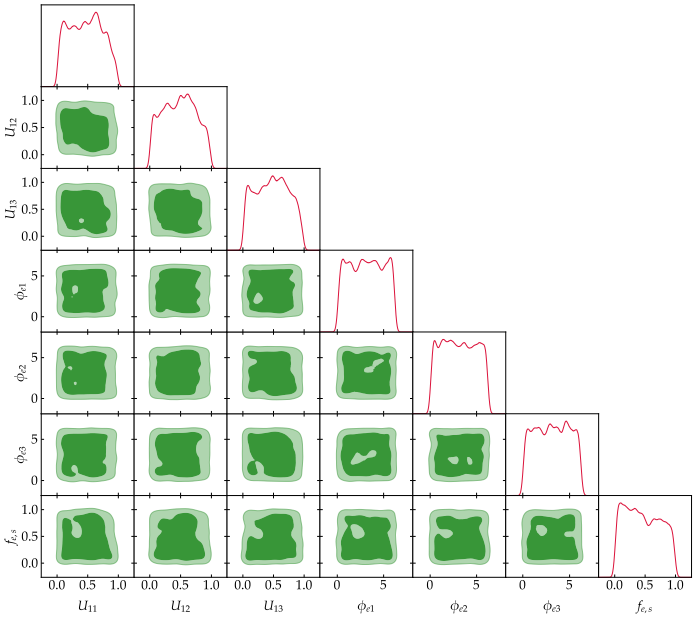

Figure 7: *Posteriors of varying parameters only in the first row (i.e. $\alpha = e$) of the U-matrix as complex numbers with a magnitude and phase as well as the initial flavour composition, $[f_{e,S}, 1-f_{e,S}, 0]$. Histograms are posterior distributions of each parameter. Green plots are correlations between the individual parameters. Dark green regions are 68% confidence regions, light green regions are 95% confidence regions.*

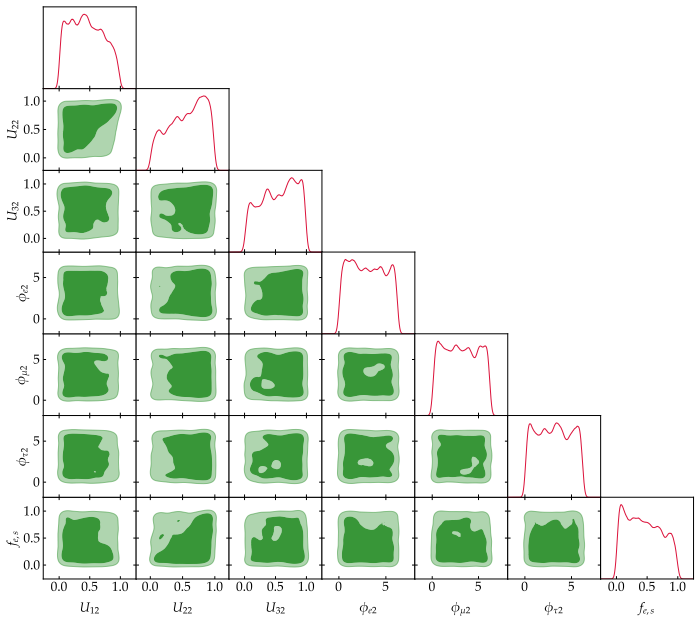

Figure 8: *Posteriors of varying parameters only in the second column of the U-matrix (i.e. $i = 2$) as complex numbers with a magnitude and phase as well as the initial flavour composition, $[f_{e,S}, 1 - f_{e,S}, 0]$. Histograms are posterior distributions of each parameter. Green plots are correlations between the individual parameters. Dark green regions are 68% confidence regions, light green regions are 95% confidence regions.*

Figs. 7 and 8 explore whether varying only a single row or column gives rise to peculiarities in the allowed matrix parameters. Perhaps one could imagine that non-unitarity appears only in the electron sector of the mixing matrix, that is, the first row. Then varying only the first row while letting the rest of the matrix take best-fit values could be a viable way to explore this possibility. The description of how to interpret these plots is given earlier on in this section. Fig. 7 does not show any signs of correlation, in general the plot looks similar to Fig. 6. Fig. 8, on the other hand, has more defined histograms. There are clearly preferred values for the parameters. This means that given our measurement at the Earth, these matrix parameters prefer to take on certain values, i.e., we can constrain these parameters more given our current measurement. Likewise, the correlation plots show that some parameters have clear constraints on them. Most notably in the second column the dark green regions do not fill out the entire square. That means that at 68% confidence these parameters cannot take on certain values together.

4.2 Unitarity Relations

In this section we will use the posteriors from section 4.1 to explore whether unitarity of U is allowed. To do this we will calculate the unitarity relations, $UU^\dagger = \mathbb{1}$, that is, we will calculate $UU^\dagger$ and see how close it is to $\mathbb{1}$. For clarity, we will write out the relations below. There are three for the diagonal,

$$\sum_i |U_{\alpha i}|^2 = 1, \quad \alpha = e, \mu, \tau, \tag{35}$$

and six for the off-diagonal,

$$\sum_i U_{\alpha i} U^*_{\beta i} = 0, \quad \alpha \neq \beta, \quad \alpha, \beta = e, \mu, \tau. \tag{36}$$

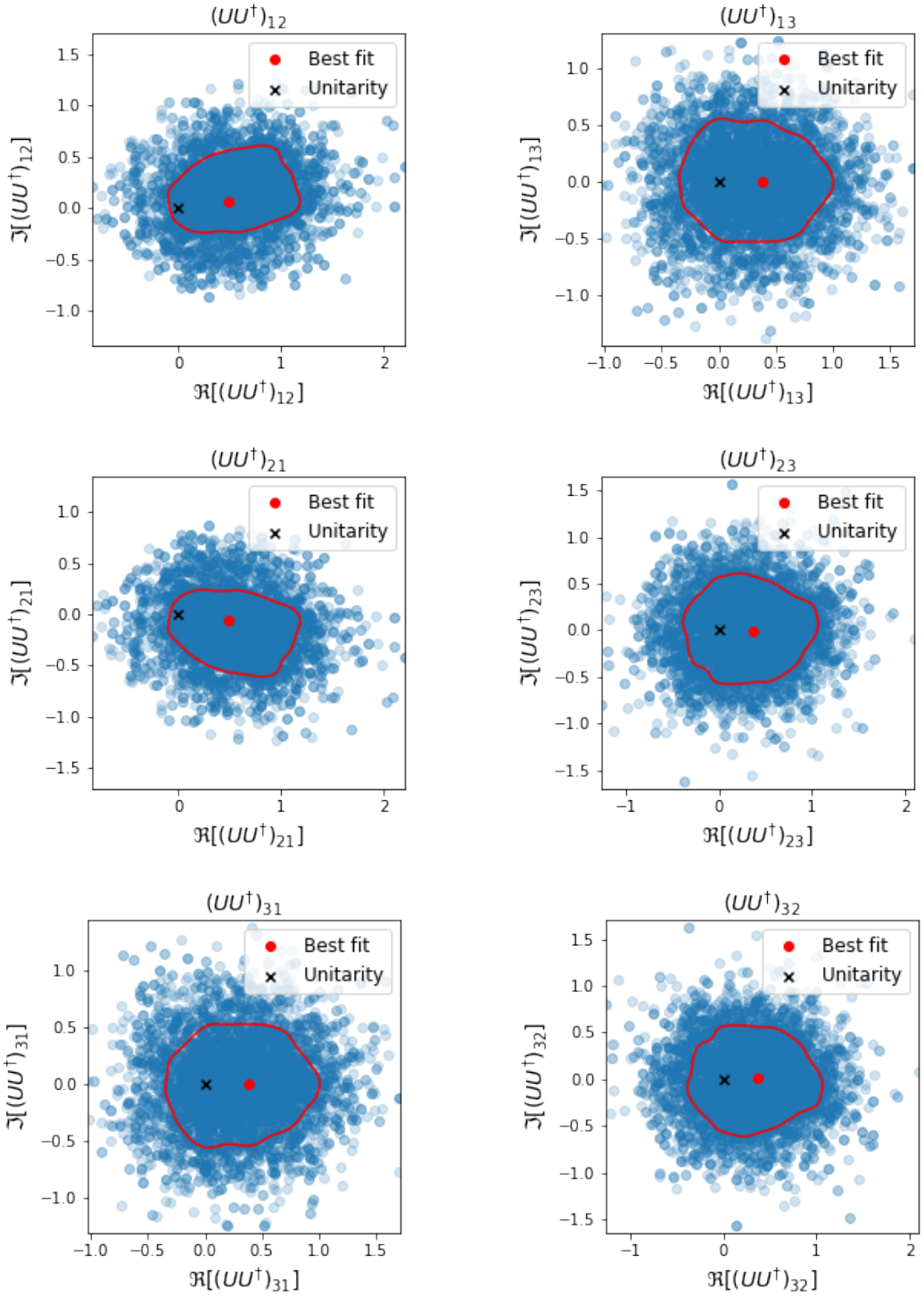

Figure 9: *Red dots denote best-fit values and red lines denote allowed regions for off-diagonal elements of $UU^\dagger$ at 68% confidence. Best-fit points are calculated from two-dimensional distributions considering the real and imaginary part of each value.*

Fig. 9 shows the posterior distributions for the off-diagonal elements of $UU^\dagger$. The blue points represent individual points in the posterior distributions of the parameters. The red dot indicates the best-fit values for these, X denotes $(0, 0)$. If U is unitary the best-fit values should be as close to $(0, 0)$ as possible. These best-fit values are not necessarily the global best fit if one considers correlations of all parameters at the same time. The red line denotes the 68% confidence region, i.e., it contains 68% of the points closest to the best-fit value. We report the norm and corresponding error of each of the off-diagonal elements of $UU^\dagger$. These are shown in Table 1. The errors are computed as the farthest possible distance between the best-fit value and the 68% contour. This is overestimating the error as it replaces the red line with a circle just touching it on its farthest away point. All the computed values are compatible with unitarity at 68% confidence.

Table 1: *Best-fit values and errors for the absolute values of the off-diagonal elements in $UU^\dagger$. For unitarity these should be 0.*

Element	Best fit	+ Error	- Error
$\lvert(UU^\dagger)_{12}\rvert$	0.485	0.703	0.485
$\lvert(UU^\dagger)_{13}\rvert$	0.384	0.733	0.384
$\lvert(UU^\dagger)_{21}\rvert$	0.485	0.703	0.485
$\lvert(UU^\dagger)_{23}\rvert$	0.366	0.760	0.366
$\lvert(UU^\dagger)_{31}\rvert$	0.384	0.733	0.384
$\lvert(UU^\dagger)_{32}\rvert$	0.366	0.760	0.366

Similarly, the errors for the diagonal elements are reported in Table 2. These are propagated using the maximum likelihood point, which is the best-fit point taking into account correlations between all parameters at the same time. This and the errors are taken directly from the UltraNest result. They are each compatible with unitarity, $(UU^\dagger)_{ii} = 1$, at 68% confidence.

Table 2: *Best-fit values and 68% confidence errors for diagonal elements of $UU^\dagger$. For unitarity these should be 1.*

Element	Best fit	+ Error	- Error
$(UU^\dagger)_{11}$	0.634	0.445	0.445
$(UU^\dagger)_{22}$	0.867	0.522	0.522
$(UU^\dagger)_{33}$	1.270	0.647	0.647

In Table 3 are the unitarity relations calculated for the analyses where only a single row or column was varied, i.e., based on the posteriors shown in Figs. 7 and 8. Errors are taken directly from these. For a unitary U these should be equal to 1.

Table 3: *Best-fit values and 68% confidence errors for unitarity relations using data from analyses where only one row or column was varied. For a unitary U these should be equal to 1.*

Unitarity relation	Best fit	+ Error	- Error
$\sum_i \lvert U_{1i}\rvert^2$	0.770	0.887	0.770
$\sum_i \lvert U_{2i}\rvert^2$	1.096	0.988	0.988
$\sum_i \lvert U_{3i}\rvert^2$	0.922	0.867	0.867
$\sum_\alpha \lvert U_{\alpha 1}\rvert^2$	1.349	1.047	1.047
$\sum_\alpha \lvert U_{\alpha 2}\rvert^2$	1.385	1.052	1.052
$\sum_\alpha \lvert U_{\alpha 3}\rvert^2$	0.722	0.892	0.722

Let us start by considering the values in Tables 1 and 2. The caveat here is that the errors, although they should yield consistent results, are calculated in slightly different ways. The values in Table 1 are calculated using the 2D best fit, taking into account only the appropriate real and imaginary component of the value we are calculating. We report the norm. Whereas in Table 3, due to the ease of calculation in not having to work with phases as they cancel out in the calculations, we have used the maximum likelihood point from the posteriors from UltraNest. To see how the cancellation happens we show an example of the calculation of $(UU^\dagger)_{11}$ below. When UltraNest reports these values, it takes into account the correlations of all parameters simultaneously. Some of these are neglected for the off-diagonal elements, however, the results should still be consistent.

When calculating

$$(UU^\dagger)_{11} = \sum_{i=1,2,3} U_{1i}U^*_{1i}, \tag{37}$$

we only sum over terms containing the amplitude squared of a given parameter. Thus, the phase cancels.

5 Discussion

It is interesting to point out that in Figs. 7 and 8 the posterior distributions of the parameter $|U_{12}|$ are very similar in the two independent fits. This means that the two different analyses yield consistent results. The same applies to the posterior distributions of ϕ_{e2} and $f_{e,S}$. However, the correlation plots between these parameters vary from simulation to simulation. This is most likely a feature of the fact that the green correlation plots are computed only from the correlation between two individual parameters, neglecting other correlations. Globally the results should be consistent.

Were we to compare the posterior distributions of the parameters in Fig. 6 to those in Figs. 7 and 8, there is a bit more freedom in the distributions of Fig. 6. Some of the same tendencies are seen but the most notable difference appears in the posterior distribution of $f_{e,S}$. In Fig. 6 it is quite flat while in Fig. 7 and 8 it is skewed towards the lower end of the range. This is a testament to the fact that when varying all 13 parameters of U there is freedom to make up for the imposed best-fit measurement value used to calculate the likelihood. However, for the simulation of varying only a row or column this is a strong enough condition such that it locks $f_{e,S}$ into certain

values. In reality we cannot measure $f_{e,S}$ directly, which is why we leave it as a model parameter, so we cannot verify whether or not the distributions match reality.

We say here that the sensitivity to the parameter $f_{e,S}$ is greater in the analysis in Fig 7 and 8, i.e., the distributions are less flat and $f_{e,S}$ has a more defined region of acceptability. The same is true if we were to rerun the analysis without renormalizing $\boldsymbol{f}_S$. We would be more sensitive to the parameters as the renormalization in effect smooths out the differences U inflicts on the flavour composition. This, of course, we cannot do, as the measurement from IceCube is by definition renormalized. In general, the analysis for a single row or column is more sensitive as it poses stricter constraints on the parameters.

Another interesting point of discussion is whether better IceCube data for $\bar{\boldsymbol{f}}_S$ would improve our simulation. Lower errors would only change the covariance matrix, σ. This would not change what values for the entries of U and $f_{e,S}$ make up the best-fit points as $\bar{\boldsymbol{f}}_\oplus$ stays the same. In theory this would make the posteriors narrower although the projected errors, which we are using, are already so low that the improvement would be negligible.

Looking at Fig. 9, one might imagine the global maximum likelihood point is different from the red dots. This is a possibility but the regions of 68% confidence, that is the red line and therefore the corresponding error should match quite well in the two cases. Overestimation of the error on the final result further strengthens this point. The conclusion of the analysis would be the same in both cases. We have chosen this approach for the error calculation as calculation of the true error is outside the scope of this project.

We could compare the diagonal elements in Table 2 with the corresponding entry in Table 3. The best-fit values are similar, all of the entries allow for 1. In general, the errors in Table 2 are smaller. This can be attributed to the analysis of more parameters at the same time. The simulation has more freedom and U is not locked at certain values.

To sum up, looking at our results, it is clear to see that our results are compatible with U being unitary, although these have large errors which are of the same order of magnitude as the best-fit results. Better simulations and more computing power could potentially produce a slight improvement; however, the issue lies rather in the fundamental difficulty in measuring the flavour composition of astrophysical neutrinos. In the analysis of varying all parameters in the LMM parametrization, because of these big errors at 68% confidence we cannot exclude the unitarity of U, i.e., $UU^\dagger$ lies within one standard deviation of $\mathbb{1}$.

The calculations of row and column unitarity relations visible in Table 3 should, if U is unitary, be equal to 1. For each of the computed relations 1 lies within the 68% confidence region. This means we cannot exclude the unitarity of U.

6 Conclusion

Our results are compatible with U being unitary, however, because of the big errors, we cannot exclude non-unitarity either. After conducting several simulations using projected data for $\boldsymbol{f}_\oplus$, we conclude the unitarity of U is allowed at 68% confidence. In the future this measurement could be optimized if we develop better neutrino telescopes that more precisely will be able to measure the flavour composition of high-energy astrophysical neutrinos.

References

[1] Boris Kayser. Neutrino physics. *eConf*, C040802:L004, 2004.

[2] M. G. et al. Aartsen. Flavor ratio of astrophysical neutrinos above 35 tev in icecube. *Physical Review Letters*, 114(17), April 2015.

[3] Neha Lad. Sensitivity of icecube-gen2 to measure flavor composition of astrophysical neutrinos, 2023.

[4] Ningqiang Song, Shirley Weishi Li, Carlos A. Argüelles, Mauricio Bustamante, and Aaron C. Vincent. The Future of High-Energy Astrophysical Neutrino Flavor Measurements. *JCAP*, 04:054, 2021.

[5] Carlo Giunti and Kim Chung Wook. *Fundamentals of Neutrino Physics and Astrophysics*. Oxford Univ., Oxford, 2007.

[6] R. L. Workman et al. Review of Particle Physics. *PTEP*, 2022:083C01, 2022.

[7] Sebastian A. R. Ellis, Kevin J. Kelly, and Shirley Weishi Li. Leptonic Unitarity Triangles. *Phys. Rev. D*, 102(11):115027, 2020.

[8] Ivan Esteban, M.C. Gonzalez-Garcia, Michele Maltoni, Thomas Schwetz, and Albert Zhou. The fate of hints: updated global analysis of three-flavor neutrino oscillations. *Journal of High Energy Physics*, 2020(9), September 2020.

[9] J.M. Bernardo and A.F.M. Smith. *Bayesian Theory*. Wiley Series in Probability and Statistics. Wiley, 2009.

[10] Stephen Parke and Mark Ross-Lonergan. Unitarity and the three flavor neutrino mixing matrix. *Phys. Rev. D*, 93(11):113009, 2016.

[11] Sebastian A. R. Ellis, Kevin J. Kelly, and Shirley Weishi Li. Current and Future Neutrino Oscillation Constraints on Leptonic Unitarity. *JHEP*, 12:068, 2020.